



Discover the beauty of standardized flow cytometry

Workflow standardization and automation made easy with the MACSQuant® Analyzer 16

Benefit from our best-in-class solutions for standardized flow cytometry. Find the perfect synergy of the right tools and be rewarded with reliable and reproducible results

- Highly specific and consistent antibodies
- Flawless instrumentation
- Automated sample labeling and acquisition
- Automated analysis and reporting software

► [miltenyibiotec.com/mq16](https://www.miltenyibiotec.com/mq16)

Miltenyi Biotec B.V. & Co. KG | Friedrich-Ebert-Straße 68 | 51429 Bergisch Gladbach | Germany
Phone +49 2204 8306-0 | Fax +49 2204 85197 | macsde@miltenyi.com | www.miltenyibiotec.com


Miltenyi Biotec provides products and services worldwide.

Visit www.miltenyibiotec.com/local to find your nearest Miltenyi Biotec contact.

Unless otherwise specifically indicated, Miltenyi Biotec products and services are for research use only and not for therapeutic or diagnostic use. MACSQuant, Tyto, the Tyto logo, and the Miltenyi Biotec logo are registered trademarks or trademarks of Miltenyi Biotec and/or its affiliates in various countries worldwide. Copyright © 2022 Miltenyi Biotec and/or its affiliates. All rights reserved.



On monocytes and lymphocytes biolens clustering by in flow holographic microscopy

Jaromír Běhal^{1,2} | Daniele Pirone^{1,3} | Daniele Sirico^{1,4} | Vittorio Bianco¹ |
 Martina Mugnano¹ | Danila del Giudice^{1,5} | Beatrice Cavina^{6,7} | Ivana Kurelac^{6,7} |
 Pasquale Memmolo¹ | Lisa Miccio¹  | Pietro Ferraro¹

¹CNR-ISASI, Institute of Applied Sciences and Intelligent Systems "E. Caianiello", Naples, Italy

²Department of Optics, Palacký University, Olomouc, Czech Republic

³DIETI, Department of Electrical Engineering and Information Technologies, University of Naples "Federico II", Naples, Italy

⁴Department of Chemical, Materials and Production Engineering of the University of Naples Federico II, Naples, Italy

⁵Department of Mathematics and Physics, University of Campania "L. Vanvitelli", Caserta, Italy

⁶Department of Medical and Surgical Sciences (DIMEC), Centro di Studio e Ricerca sulle Neoplasie (CSR) Ginecologiche, Alma Mater Studiorum-University of Bologna, Bologna, Italy

⁷Centre for Applied Biomedical Research (CRBA), University of Bologna, Bologna, Italy

Correspondence

Lisa Miccio, CNR-ISASI, Institute of Applied Sciences and Intelligent Systems "E. Caianiello", Via Campi Flegrei 34, 80078 Pozzuoli, Naples, Italy.
 Email: lisa.miccio@cnr.it

Funding information

MIUR PRIN 2017 - Morphological Biomarkers for Early Diagnosis in Oncology (MORFEO), Grant/Award Number: Prot. 2017N7R2CJ

Abstract

Live cells act as biological lenses and can be employed as real-world optical components in bio-hybrid systems. Imaging at nanoscale, optical tweezers, lithography and also photonic waveguiding are some of the already proven functionalities, boosted by the advantage that cells are fully biocompatible for intra-body applications. So far, various cell types have been studied for this purpose, such as red blood cells, bacterial cells, stem cells and yeast cells. White Blood Cells (WBCs) play a very important role in the regulation of the human body activities and are usually monitored for assessing its health. WBCs can be considered bio-lenses but, to the best of our knowledge, characterization of their optical properties have not been investigated yet. Here, we report for the first time an accurate study of two model classes of WBCs (i.e., monocytes and lymphocytes) by means of a digital holographic microscope coupled with a microfluidic system, assuming WBCs bio-lens characteristics. Thus, quantitative phase maps for many WBCs have been retrieved in flow-cytometry (FC) by achieving a significant statistical analysis to prove the enhancement in differentiation among sphere-like bio-lenses according to their sizes (i.e., diameter d) exploiting intensity parameters of the modulated light in proximity of the cell optical axis. We show that the measure of the low intensity area ($S: I(z) < I_{th}(z)$) in a fixed plane, is a feasible parameter for cell clustering, while achieving robustness against experimental misalignments and allowing to adjust the measurement sensitivity in post-processing. 2D scatterplots of the identified parameters (d - S) show better differentiation respect to the 1D case. The results show that the optical focusing properties of WBCs allow the clustering of the two populations by means of a mere morphological analysis, thus leading to the new concept of cell-optical-fingerprint avoiding fluorescent dyes. This perspective can open new routes in biomedical sciences, such as the chance to find optical-biomarkers at single cell level for label-free diagnosis.

KEYWORDS

biolens, digital holographic cytometry, microfluidics, opto-biology, white blood cells

This is an open access article under the terms of the [Creative Commons Attribution-NonCommercial-NoDerivs](https://creativecommons.org/licenses/by-nc-nd/4.0/) License, which permits use and distribution in any medium, provided the original work is properly cited, the use is non-commercial and no modifications or adaptations are made.

© 2022 The Authors. *Cytometry Part A* published by Wiley Periodicals LLC on behalf of International Society for Advancement of Cytometry.

1 | INTRODUCTION

Common biological samples exhibit high transmission in the visible spectral range, thus assimilating the surrounding background naturally. Hence, low-contrast images appear in a standard light microscope under visible illumination. Such a poor contrast is typically enhanced by changing absorbance via sample staining or employing more sophisticated optical methods, including Quantitative Phase Imaging (QPI) techniques [1].

Recently, it has been found that biological samples behave as optical elements. The essential biophotonic probes, based on a single-cell hierarchy, include biolasers, waveguides, and biolenses [2,3]. Ambition for integrating these elements into the performance of photonics arises from the need for such biocompatible and available micro components. Lasing on a single-cell level was first introduced in living cells, including green fluorescent protein, which served as a gain medium [4].

Furthermore, it was proved that many cell types, including Red Blood Cells (RBCs), exhibit the biolensing effect and thus can behave as active micro-lenses, characterized by flexible focal lengths and magnifications, making them available for many applications, for example, imaging, light coupling, and lithography [5–7]. Recently, methods to overcome the optical diffraction limit aimed at realizing super-resolution imaging have been developed employing biological samples [8,9]. Such a concept is useful for diagnosis at single-cell level. In fact, changes in biolens performance can be correlated directly to the living cell morphology and to the typical biochemical activities [10–14].

Nevertheless, diagnostics at cellular level need large-scale analysis to get statistically significant data for classification, which can be obtained incorporating high-throughput in-flow working modality. Many commercially available flow cytometers exist. One of the most widespread is the Fluorescent-Activated Cell Sorter (FACS), which achieves high sorting accuracy by combining morphological parameters and fluorescence. However, in FACS the studied cells must undergo the antibody labeling process which is invasive and can affect downstream analysis of ordered populations [15]. Consequently, many efforts have been spent in developing label-free methods for analysis to be exploited in flow cytometry [7,16–20]. Among them QPI is one of the investigated detection modalities due to the great amount of information enclosed in the phase-contrast map of biological matter [21,22]. In particular, in Reference [23] authors used in-line Digital Holography (DH) and the analysis of the maximal in-focus intensity for fingerprinting cells of similar sizes while differing in the Refractive Index (RI) distribution. A classification approach was proposed afterwards by the same group [24] incorporating size, maximum intensity, and mean intensity as features for machine-learning based classification. One of the main advantages of off-axis DH approaches over one-arm in-line DH is the possibility to introduce a fringe carrier modulated in amplitude and phase by the sample. The visibility of the fringes is tunable in off-axis DH, for example, by optimizing the power

balance between the object and reference beams or acting on their polarization states. In turn, off-axis setup allows optimizing the contrast of the diffraction pattern of out-of-focus specimens. Conversely, in in-line DH, the sample signal contrast strictly depends on the acquisition plane and the sample features. Hence, for in-line DH microfluidic experiments, the sample axial position inside the channel affects the contrast and results in variable accuracy in 3D tracking and determining the maximal in-focus intensity, which could be one of the possible reasons for the large coefficients of variance reported in Reference [23].

The possibility to combine in collaborative manner scattering analysis and holographic imaging for flowing monocytes (MCs) and lymphocytes (LCs) has been investigated also by Dannhauser and co-workers [25–27] to check the position of individual cells and to estimate their 3D morphometric features, such as their RI.

Among QPI imaging, a recent valuable paper by D. R. Steike and co-workers demonstrates that biophysical and morphological features calculated in static mode by DHM apparatus (i.e., cell volume, refractive index, dry mass, and cell shape related form factor) are in good agreement with common flow cytometric cell markers in a prospective observational pilot study on patients before and after cardiac surgery [28].

Here we propose a different approach where an off-axis digital holographic flow cytometer provides the identification of two different populations by analyzing the intensity spots in the focusing region and simultaneously supplies the quantitative phase-contrast images of the cells. The method is applied to WBCs, that is, a heterogeneous population consisting of several cell-types which can be mainly categorized as mononuclear and polymorphonuclear cells. Mononuclear cells include MCs and LCs, which are similar in RIs [29] but different in sizes.

The primary motivation of this work is to enhance the differentiation among sphere-like biolenses according to their sizes by using intensity parameters of the modulated light. Notably, MCs and LCs are observed inflow and treated as micro-size biolenses. The proof of principle experiment exploits the advantages of DH, that is, a non-invasive coherence-based imaging technique that retrieves the complex amplitude of the investigated object and allows its refocusing [30]. Firstly, cells are characterized according to their quantitative phase maps. Subsequently, the complex amplitude is propagated numerically, and the imaging characteristics are evaluated from the intensity profile in proximity of the cell optical axis. In particular, we show that the measure of the low intensity area, in a fixed plane, is a feasible parameter for cell clustering, while performing robustness against experimental misalignments and allowing to adjust the measurement sensitivity in post-processing, simultaneously. As a general pathway, we believe that characterizing the biolensing properties of WBCs, herein exploited for automated classification, will lay the foundations for further downstream analysis, WBCs phenotyping, and for defining the levers to activate to use them as imaging boosters in lab on a chip device emulating complex biological systems.

2 | METHODS

2.1 | Sample preparation

These experiments were performed by using monocyte cell line THP-1 and human T lymphocyte cells Jurkat. THP-1 cells were cultured as suspension cells in T-flasks using RPMI-1640 Medium, (Life technologies, ref 31870-025) supplemented with 10% fetal bovine serum (FBS) (Sigma, St. Louis, MO), 2 mM L-Glutamine (Lonza, Cat N.: BE17-605E) and 1% Penicillin/Streptomycin (Lonza, Cat N. DE17-602E), and maintained in cell culture flask (Corning, product number 353018) at 37°C in a humidified atmosphere with 5% CO₂. The day of the experiment they were harvested from the cell culture flask and transfer into a centrifuge tube containing 7.0 ml complete growth medium and spin at approximately 125×g for 5 min, resuspended in complete medium and injected into the microfluidic channel at final concentration of 2 × 10⁵ cells/ml. The Jurkat medium was formulated using RPMI 1640 Medium (Euroclone #ECB9006L), to make the complete growth medium was added 20% FBS (Euroclone #ECS5000L), 2 mM L-Glutamine (Lonza, Cat N.: BE17-605E) and 1% Penicillin/Streptomycin (Lonza, Cat N. DE17-602E). The T lymphocyte cells support the suspension phenotype and were cultured in 25 cm² flasks. For the purpose of obtaining the final cell concentration of 2 × 10⁵ cells/ml, the cells were harvested from the flask and centrifuged for 5 min at 1000 rpm, thus were resuspended in their medium. The cell's viability of the 90% was proved by Typan Blue (Sigma T8154) viability assay.

2.2 | Experimental arrangement

The experimental setup is based on the geometry of the Mach-Zehnder interferometer (Figure 1A), where a laser beam (λ = 532 nm, Laser Quantum Torus 532) is split into two independent optical paths: the reference and signal arms, respectively. The light in the signal arm illuminates the microfluidic channel (MC; Microfluidic ChipShop 10,000,107–200 μm × 1000 μm × 58.5 mm) containing the sample, and is transmitted by the microscope objective (MO; Zeiss Plan-Apochromat 40×, NA = 1.3, oil immersion) toward the tube lens (TL; effective focal length 150 mm) and camera (CAM; Genie Nano-CXP Cameras, 5120 × 5120 pixels, 4.5 μm square pixels), thus reaching ≈36× magnified imaging performance. Constant cell flow of the sample is controlled employing the syringe pump system (CETONI Syringe Pump neMESYS 290N) which is connected to the MC by PTFE capillaries. The syringe pump system provides a flow rate equal to 50 nl/s, that guarantees a translational velocity in the range of 80–100 μm/s inside the microfluidic chip. Finally, a collimated beam emerging from the reference arm is mixed with the signal beam via a beam-splitter cube (BS) placed in front of the camera detecting the snapshot interference record at exposure time set to 34 μs. WBC density is about tens of well-separated cells in a Field-of-View (FoV) of 650 μm × 650 μm. Detailed description of the implemented experimental arrangement can be found in Reference [31].

2.3 | Hologram processing

As the snapshot hologram (Figure 1B) arises from the mixture of mutually coherent optical fields, it can be expressed as

$$H = |U_S|^2 + |U_R|^2 + U_S U_R^* + U_S^* U_R. \quad (1)$$

The first two terms $|U_S|^2$ and $|U_R|^2$ represent intensities of the signal and the reference waves, and the asterisk * stands for a complex conjugation. Separation of the holographic terms $U_S U_R^*$ and $U_S^* U_R$ from the zero-diffraction order is feasible if spatial frequencies $\frac{\cos \theta_{kl}}{\lambda}$, $l = \{x, y, z\}$, carried by the reference wave are sufficiently high. Meeting the previous conditions, the recorded hologram was Fourier transformed, the valuable diffraction order was isolated, and the spatial carrier frequency was removed. The modified spectrum was inverse Fourier transformed and the retrieved complex amplitude was employed for a single cell-detection inside the observed Field of View (FoV). Area of ≈48×48 μm² containing a single cell in its center was subsequently established and used for further calculations. Cells identification inside the FoV is operated manually. In particular, the angular spectrum approach was used for the complex-amplitude propagation [32]. Moreover, the Tamura Coefficient (TC) [33].

$$TC = \sqrt{\frac{\sigma(l)}{\langle l \rangle}}, \quad (2)$$

where σ stands for a standard deviation and $\langle \cdot \rangle$ for an average value, was applied on intensity profile l in each defocused axial distance. Axial position corresponding to the focal plane of each cell z_{TCmin} was subsequently found inside the evaluated area as a position where TC reaches its minimum. Amplitude and phase-maps obtained after such a procedure are illustrated in Figure 1C,D, where a “low” contrast image is evident for the amplitude-map. Axial positioning, as well as amplitude and phase map calculations are automatically retrieved for the all WBCs by home-made software suite realized on MATLAB.

2.4 | Focusing fingerprint by sphere-shaped lenses

Observation of unstained biological samples by light microscope in the object plane is challenging due to their high transparency in the visible region (Figure 1C). However, we noticed that flowing round-shaped cells inside the MC can be represented as flowing high-intensity spots in the defocused planes (Figure 1E). It is expected that transparent particles distinct in size may differ also in their focusing properties. Notably, a sphere of refractive index n , the diameter d , surrounded by medium of refractive index n_K , and distant l from borders with the air behaves as a lens with focal distance f (Figure 2A) given as

$$f = \frac{nd}{4(n - n_K)} \frac{1}{n_K} + l \left(1 - \frac{1}{n_K} \right), \quad (3)$$

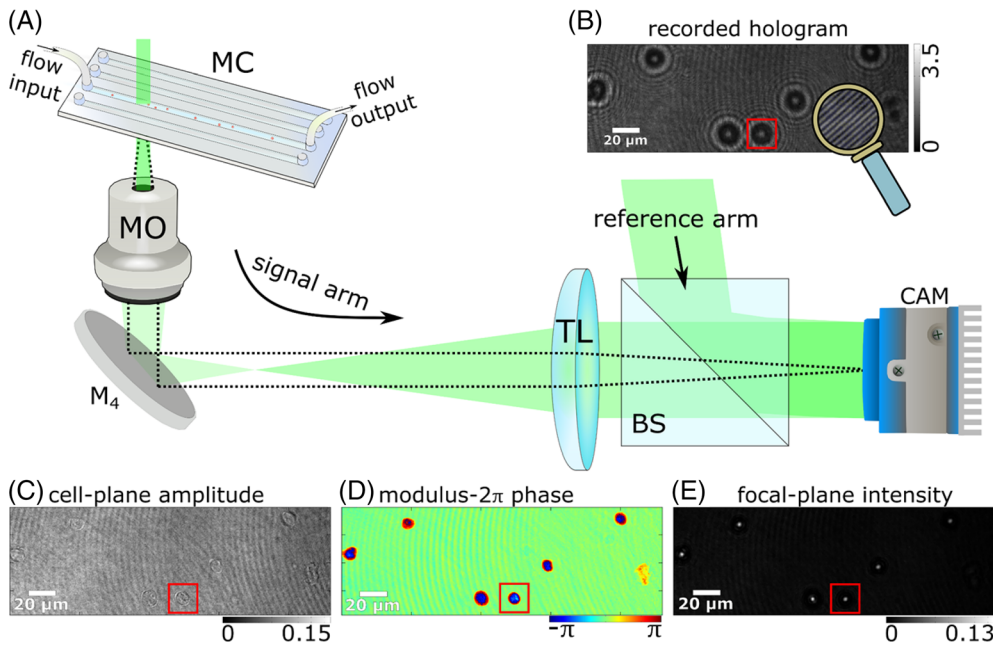


FIGURE 1 (A) Simplified sketch of used experimental arrangement. (B) Selected part of the interference snapshot. (C) Overall cell-plane amplitude. (D) Modulo- 2π phase in the overall cell plane. (E) Focal-plane intensity [Color figure can be viewed at wileyonlinelibrary.com]

which can be for small distances l (in comparison to the first term) approximated as

$$f \approx \frac{nd}{4(n-n_K)} \frac{1}{n_K}. \quad (4)$$

It means that larger spheres of equal n exhibit longer focal distances than the smaller spheres if $(n - n_K) > 0$.

Here, the propagated complex amplitude was investigated to compare focal distances of LCs and MCs. The cell plane was found as the axial coordinate z_{TCmin} where TC, calculated for intensity, reaches the minimum. Subsequently, the image plane was localized as the distance z_{TCmax} where TC reaches its maximum [33]. Thus, the focal distance f_{TC} was calculated based on the pure contrast measure as a difference between these two planes

$$f_{TC} = z_{TCmax} - z_{TCmin}. \quad (5)$$

Secondly, the focal distance f_{Imax} was calculated as a distance between the plane z_{TCmin} and the plane of maximal intensity z_{Imax} (i.e., the plane, where intensity reaches its global maximum) by the formula

$$f_{Imax} = z_{Imax} - z_{TCmin}. \quad (6)$$

To enhance a robustness of data processing, the position z_{Imax} of maximal intensity I_{max} can be assessed as it is described in the following. Firstly, cell-complex amplitude is propagated by distance z_0 using angular spectrum approach [32]. Moreover, the circular mask of diameter $22 \mu\text{m}$ is set to separate intensity contributions of a single cell from surroundings. Maximal intensity $I_{max}(z_0)$ in the current plane z_0 is further evaluated as a median of 100 highest-intensity pixels

present inside this aperture. Calculations are accomplished for all assumed axial positions z . Finally, the maximal intensity I_{max} represents maximum from the vector $I_{max}(z)$, that is, $I_{max} = \max(I_{max}(z))$, and the position z_{Imax} corresponds to the plane where $z = z_{Imax}$ for which it is valid that $I_{max}(z_{Imax}) = I_{max}$. In Figure 2B f_{TC} and f_{Imax} are showed for one LC and one MC respectively.

Moreover, we define threshold intensity $I_{th}(z)$ according to equation

$$I_{th}(z) = c I_{max}(z), \quad (7)$$

where $c \in (0, 1)$ is a constant. It can be noticed that $I_{th}(z)$ is for the same c higher in the case of cells providing the higher intensity in the current plane in comparison to cells producing less intensity. Consequently, the coefficient c defines the area S where $I(z) < I_{th}(z)$.

2.5 | Separation of two distributions

The separation between two one-dimensional distributions of the parameter of interest d (representing diameter of cells in the following text) calculated for MC and LC populations can be quantified by the coefficient

$$g_d = \frac{|\langle d_M \rangle - \langle d_L \rangle|}{\sigma(d_M) + \sigma(d_L)}, \quad (8)$$

where the operator $\langle \dots \rangle$ denotes a mean value and $\sigma(\dots)$ represents the standard deviation. The coefficient g_d thus expresses distance between mean values of the two distributions relative to the sum of their standard deviations. Consequently g_d represents relative distance between diameter-distributions of monocytes (d_M) and

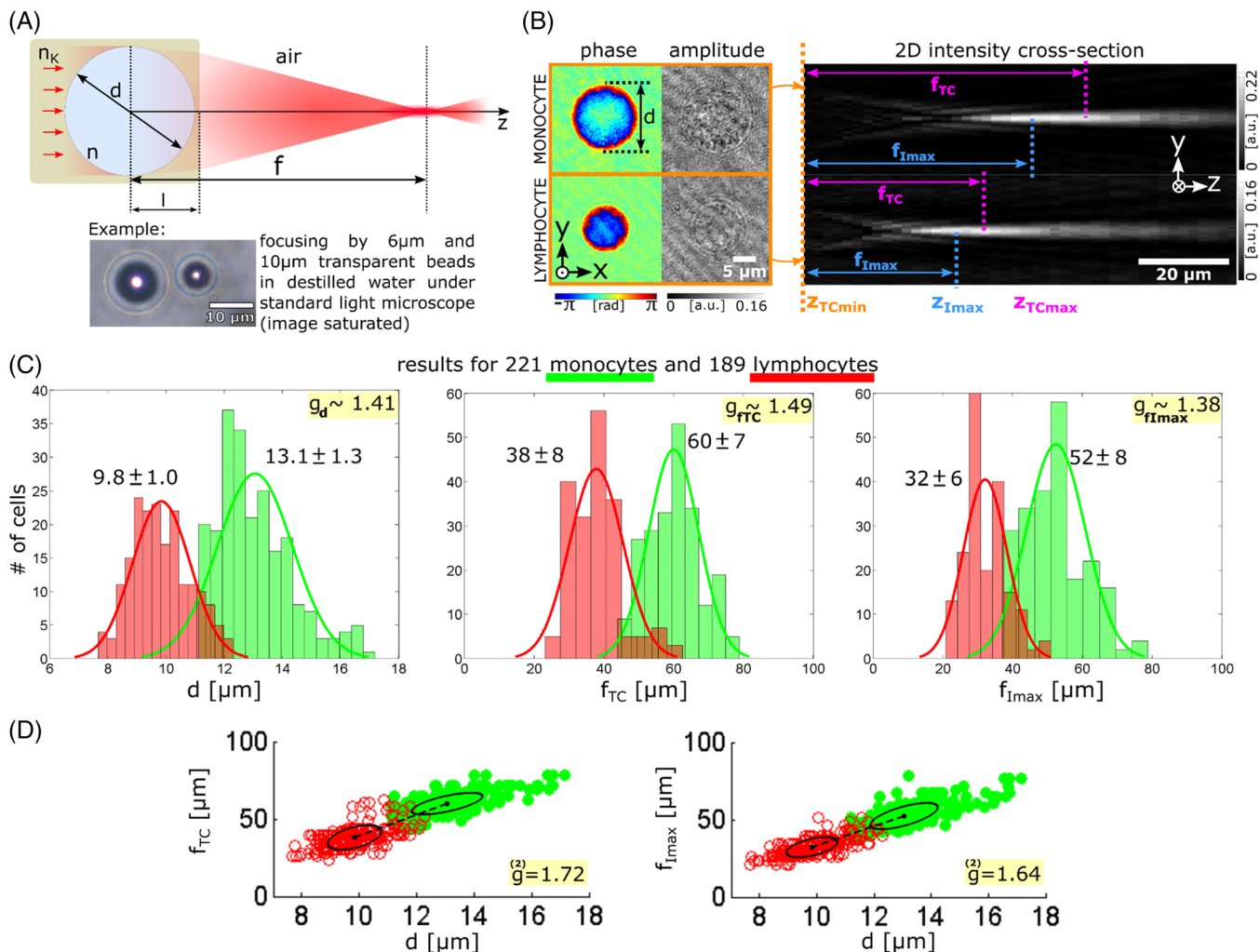


FIGURE 2 (A) Focusing by micro-spheres. (B) Amplitude and phase profiles of round-shaped cells and the propagated intensity profiles. (C) Distributions of diameter d , focal distance f_{TC} , and focal distance $f_{I_{max}}$. (D) Scatter plots $d - f_{TC}$, and $d - f_{I_{max}}$. Present ellipses fitted to each of the distributions separately are centered in the mean values of the distributions and their borders define the distance of one standard-deviation. The number $-g^{(2)}$ represents the relative distance between both 2D distributions. Detailed description of the parameter $g^{(2)}$ is provided in the main text [Color figure can be viewed at wileyonlinelibrary.com]

lymphocytes (d_L). In the following text we will evaluate this coefficient “ g ” also for the other parameters representing the two populations; namely: (i) focal distance f_{TC} calculated according to TC, (ii) focal distance $f_{I_{max}}$ calculated according to position of maximal intensity (I_{max}), and (iii) for the area S where intensity is lower than set threshold. Correct meaning of these parameters is explained in the following text.

3 | RESULTS AND DISCUSSION

Motivation to treat LCs and MCs as micro-biolenes seems to be straightforwardly applicable for their differentiation in size (Figure 2B). Diameters calculated from the cell profiles for 189 LCs and 221 MCs confirm diverse distributions, in particular with average values equal to $9.8 \pm 1.0 \mu\text{m}$ for LCs and $13.1 \pm 1.3 \mu\text{m}$ for MCs

(Figure 2C). In such a case, the distance between diameter-distributions of LCs and MCs reaches $g_d = 1.41$. Moreover, focal distances calculated by the Equation (4) for retrieved cell-diameters, refractive index of cells $n = 1.38$, and surrounding medium $n_k = 1.33$ reach $f = 51 \mu\text{m}$ in case of LCs and $f = 68 \mu\text{m}$ for MCs, thus offering possibility for the cell discrimination. Focal distance f_{TC} calculated from data reach $38 \pm 8 \mu\text{m}$ for LCs and $60 \pm 7 \mu\text{m}$ for MCs. On the other hand, focal distance $f_{I_{max}}$ reaches $32 \pm 6 \mu\text{m}$ for LCs and $52 \pm 8 \mu\text{m}$ for MCs. It was anticipated that f_{TC} , regarding the focal distance based on the contrast measure, and $f_{I_{max}}$, considering the position of maximal intensity, may differ. Displacement of maximal intensity out of the paraxial image is frequently induced by optical aberrations [34] or/and the Focal Shift (FS) effect [35]. FS appears because of diffraction in low-Fresnel-number ($N_f = \frac{(d/2)^2}{\lambda f}$) imaging systems and is coupled with asymmetric axial point-spread function (PSF) [36] as is typical for micro-lenses applications [37]. In this case,

typically valid for cells ($N_f \approx 1$), the position of the highest intensity is not located at the paraxial image plane z_{TCmax} but it is shifted $\approx -0.40f$ toward the cell. Similarly, the maximum-intensity displacement due to spherical aberration can be evaluated according to the approximative Strehl's criterium as $\approx 2A_{040}/NA^2$ [32] providing a maximal-intensity shift $\approx -0.25f$ for the considered cell-sizes and common values of RI of cells 1.38 and surrounding medium 1.33 [38]. Finally, it can be observed that separation between diameter-distributions of LCs and MCs ($g_d = 1.41$) is proportional to the separation between distributions of f_{TC} and f_{lmax} ($g_{fTC} = 1.49$, $g_{f_{lmax}} = 1.38$; Figure 2C), which can be observed also in the scatter plots $d - f_{TC}$, and $d - f_{lmax}$ (Figure 2D). However, assessment of focal distances of cells can be challenging when considering non-holographic measurements.

In Figure 2A two polystyrene microbeads of $6 \mu\text{m}$ and $10 \mu\text{m}$ diameters in aqueous suspension (Sigma-Aldrich) are imaged by a standard light microscope in the plane defocused toward the focal

spots. As most light is focused inside a tiny spot in the lateral plane, the dark area arises following the silhouette of microbeads. Such micro-lenses concentrate most of the energy into volume significantly spread along the optical axis of dimensions, scaling with $\sim 1/NA$ in the lateral direction and $\sim 1/NA^2$ in the axial direction. Since the numerical aperture $NA \approx \frac{d}{2f} = 2(n - n_K) \cdot n_K/n$ is independent of the microbead's diameter, the size of a high-intensity spot for a given wavelength depends on spherical aberration, extending the spot size for bigger particles, and the defocusing distance. However, the axial distance between two first intensity minima in proximity to the focal plane, calculated according to the approximative formula $2\Delta z_0 = 4\lambda/NA^2$, exceeds $200 \mu\text{m}$ predicting a large Depth of Focus (DoF).

Indeed, high-intensity spots follow cell positions along an extended range of axial distances (Figure 2B) and allow the cell tracking without need for contrast agents. Hence, further evaluations are related to the sequential axial scanning where established parameters arise from the current-plane intensity profile only. Firstly the maximal

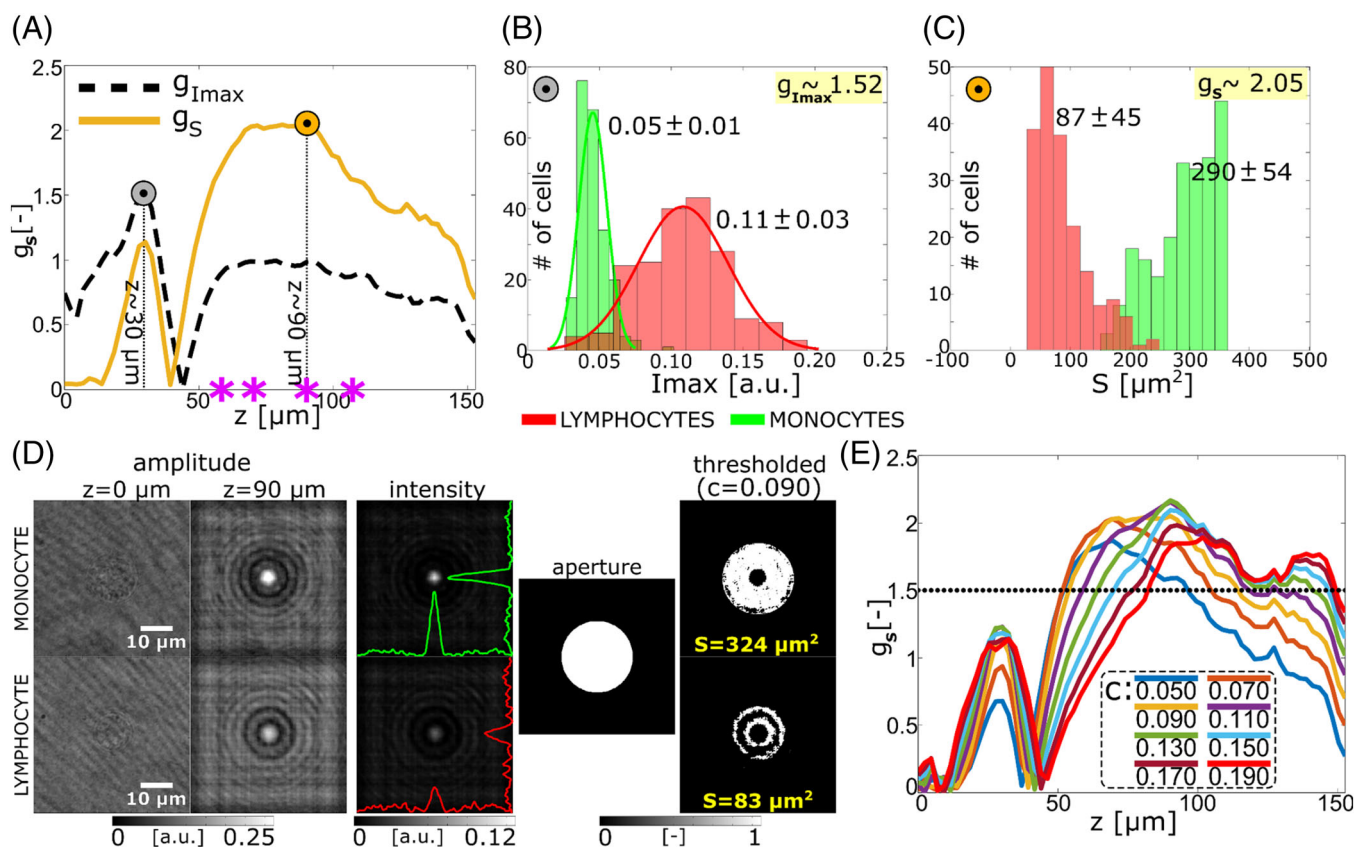


FIGURE 3 (A) Dependency of g_{lmax} on z , that is, distance between distributions of axially dependent maximal intensity $S_{lmax}(z)$ evaluated in the current lateral plane $z = z_0$ (black dashed line). Dependency of g_s on z , that is, distance between distributions of the area S evaluated in the current lateral plane $z = z_0$ (orange line). (B) Distributions of $I_{max}(z)$ evaluated in the lateral plane $z = z_0 = 30 \mu\text{m}$. (C) Distributions of S evaluated in the lateral plane $z = z_0 = 90 \mu\text{m}$. (D) Example of estimation of the area S for two selected cells. Amplitude in the cell-plane, amplitude in the $90 \mu\text{m}$ defocused plane, the corresponding intensity profile, circular aperture, and evaluated area S for $c = 0.090$. The coefficient c determines the portion of the maximal intensity I_{max} (established in the current lateral plane $z = z_0$) to set the thresholding limit I_{th} according to Equation (7). Defocused amplitude for a monocyte is slightly saturated for better visualization. (E) Axial dependence of g_s for different values of the coefficient c . [Color figure can be viewed at wileyonlinelibrary.com]

intensity $I_{\max}(z)$ in the current plane was assumed. The distributions obtained for LCs and MCs were further used to calculate the separation coefficient g_{\max} (Equation (8)). Hence, the dependence of g_{\max} on z can be observed in (Figure 3A), reaching maximum in the plane $z = 30\mu\text{m}$ where $g_{\max} = 1.52$ (Figure 3B), thus slightly exceeding the separation of diameters (Figure 2C). It can be noticed that the plane $z = 30\mu\text{m}$ lies in proximity to the plane of LCs maximal intensity ($f_{\max} = 32 \pm 6\mu\text{m}$). Limitation of such an approach arises from narrow range of axial distances where g_{\max} exceeds ≈ 1.4 , thus being sensitive to experimental inaccuracies.

Moreover, the axial dependency $g_{\max} - z$ allows to set different threshold limits for variously focusing particles. It can be noticed that $I_{\text{th}}(z)$ is for the same c higher in the case of cells providing the higher intensity in the current plane in comparison to cells producing less intensity. Initially, $c = 0.090$ was set to estimate area S inside the circular mask, where $I(z) < I_{\text{th}}(z)$. The calculated distributions obtained for LCs and MCs were further used to calculate g_s . The dependence of g_s on z is shown in the plot of Figure 3A, reaching maximum in the plane $z = 90\mu\text{m}$ where $g_s = 2.05$. Meaning of the area S can be understood from an example in Figure 3D, where results obtained for cells from Figure 2B are present. Cells are firstly defocused by $90\mu\text{m}$ from their initial planes. The calculated intensity profiles are further apertured and thresholded (Equation (7)) assuming $c = 0.090$. The area S then reaches $324\mu\text{m}^2$ for the monocyte and $83\mu\text{m}^2$ for the lymphocyte, respectively.

Moreover, the value of the coefficient c was changed in the range $c \in (0.050; 0.190)$ (Figure 3E). In all the assumed cases the limit $g_s = 1.5$ was exceeded in an extensive axial range at least $\approx 50\mu\text{m}$, which tends to be shifted toward longer distances with the increasing c . Simultaneously, the optimal detection plane is always set in proximity or farther from the focal plane expected for cells of larger

diameter. It is worth pointing out that this tolerance to changes of c and large DoF reduces requirements for precision of the experimental settings.

It should be noted that the value $g_s = 2.05$ (Figure 3A) does not necessarily mean improving the clustering accuracy in comparison to the classification based on cell diameters. More importantly, cells overlapping in diameters also overlap in the proposed evaluations; thus, it was found that the area S follows the cell-diameter dependency (see scatterplots in Figure 4). Ellipses present in Figure 4 were retrieved by fitting and defining the distance of one standard-deviation with respect to the position of mean value of the 2D distribution, that is, position of the mean value is in the center of the corresponding ellipse. Relative distance between d - S distributions of monocytes and lymphocytes thus must be calculated considering the standard-deviation angular dependency because value of the standard deviation depends on the orientation angle in which it is calculated. Generalized version of the parameter “ g ” (Equation (8)) into 2D (noted as $g^{(2)}$ in the corresponding images) contains the Euclidean distance, abscissa, between centers of the two ellipses in the numerator and sum of two standard deviations in the denominator. Each of the considered standard deviations is determined as a distance between the ellipse center and the cross-section of the abscissa with the ellipse. Values of $g^{(2)}$ belong to the range $[\sim 1.8 - 2.4]$ hence enhancing the differentiation with respect to the 1D case (Figure 3E).

It can be highlighted that results presented in Figure 4 pave the way to a method where cells are characterized according to their diameters in dependence of the defocusing distance z and thresholding coefficient c . Graphs contain a linear part at the central range and saturation at the borders, where the evaluated areas reach their minimum and maximum values, the latter being approximately determined by the size of the enclosing circular aperture. The linear parts of

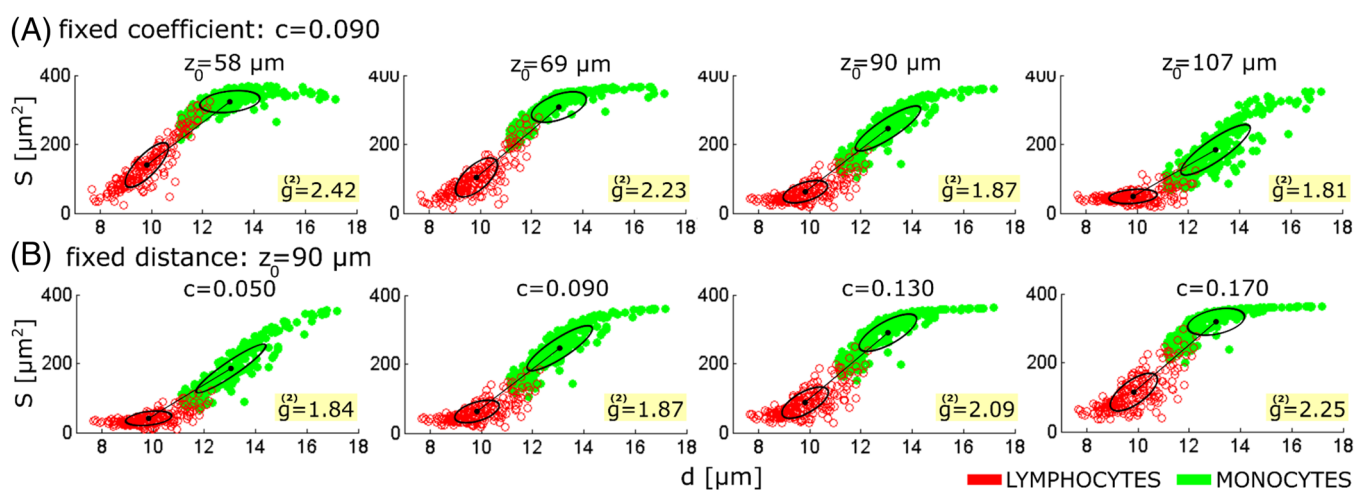


FIGURE 4 The coefficient c determines the portion of the maximal intensity I_{\max} (established in the current lateral plane $z = z_0$) to set the thresholding limit I_{th} according to Equation (7). (A) d - S dependency in the planes defocused by $z_0 = 58\mu\text{m}$, $z_0 = 69\mu\text{m}$, $z_0 = 90\mu\text{m}$, and $z_0 = 107\mu\text{m}$ (marked by purple asterisks in Figure 3A) for a fixed value $c = 0.090$. (B) d - S dependency for different coefficients $c = 0.050$, $c = 0.090$, $c = 0.130$, $c = 0.170$ in the fixed defocusing plane $z_0 = 90\mu\text{m}$. The fitted ellipses are centered in the mean values of the distributions and their borders define the distance of one standard-deviation. The number $g^{(2)}$ represents the relative distance between both 2D distributions. Detailed description of the parameter $g^{(2)}$ is provided in the main text [Color figure can be viewed at wileyonlinelibrary.com]

graphs exhibit the highest slope which is the most sensitive to changes of the assumed parameters. One of the experimentally important conclusions is the robustness of this classification method against axial misalignments which is illustrated in Figure 4A where the d - S dependency is accomplished for various defocusing distances, that is, $z = 58 \mu\text{m}$, $z = 69 \mu\text{m}$, $z = 90 \mu\text{m}$, and $z = 107 \mu\text{m}$, respectively, while $c = 0.090$ remains constant. It is observed that bigger cells move toward the linear part of the graph with the increasing distance z . In addition, the comparable performance is achieved using different values of the thresholding coefficient c for measurements accomplished in the fixed plane (Figure 4B). In this case, smaller cells move toward the linear part with increasing c . This property principally allows to adjust sensitivity of the measurement by acting on c while avoiding the need for scanning. This d - S dependence can be employed to assess diameter of the investigated cell as a function of the measured area S .

Possible future applications of the presented results would be in the field of label-free discrimination of different cell populations in cytometric approach [39–41]. There is a great demand in finding morphological biomarkers that avoid the use of fluorescent labels in order to reduce the time consumption of sample preparation and also avoid phototoxicity to allow faster and more efficient downstream analysis. Bio-lens modeling would be a valuable route to marker-free samples clustering because the focused light encodes information both on shape and refractive index distribution inside the cell-volume. Such modeling would in principle avoid the feature calculation from the whole bi-dimensional phase-map as in Reference [28]. Indeed, a realistic implementation of a cytometer based on bio-lensing properties does not necessary need the whole DH image processing pipeline but it would be necessary the recording of the intensities by putting the camera in a well-defined range of distances and propagating the field at a nominal distance thus strongly reducing the processing time. Sensitivity of measurements can be set according to expected cell-size distributions (Figure 4B) and varied in the post processing. In order to allow a realistic implementation of the proposed strategy in real word applications, some improvements in the microfluidics module and automated data processing are necessary. It would be desirable a microfluidic focusing solution to achieve the exact axial positioning of each cells present in an ensemble, thus avoiding the numerical step of sample refocusing. Automated cell detection for synchronizing the recording is also necessary to optimize the measurements and their storage. The use of Artificial Intelligence would speed up the entire processing to allow video rate image analysis. In the optimized system the expected throughput for data acquisition would be potentially the same of current image flow cytometers (thousands of cells per second). Moreover, also cell sorting would be feasible when video rate image analysis is supported by AI as already proved in References [42–45].

4 | CONCLUSION

We proposed a label-free optical method to identify suspended cells of similar refractive index, which was tested on two types of white

blood cells that differ in size, that is, lymphocytes and monocytes, respectively. Such micro bio-lenses concentrate most of the passing-through light into bright spots of significant depth of focus. Notably, the high-intensity volume was retrieved, and calculations at various defocusing distances were accomplished near the optical axis. The resulting thresholded-intensity area was evaluated, whose proportionality to cell diameter was confirmed. Since the approach works efficiently in an extended range of defocusing distances, it exhibits tolerance against axial misalignments. Additionally, specific experimental settings were discussed, proposing conditions for adjusting the evaluation sensitivity even without the need for the whole DH pipeline processing thus enhancing the throughput and speeding up the computational image analysis. Microfluidic strategies for cell focusing and AI assisted image analysis would support possible future implementation of the proposed approach. The results show that the optical features tested on white blood cells can be exploited in biomedical sciences as optical biomarkers for label-free characterization.

ACKNOWLEDGMENT

Open Access Funding provided by Consiglio Nazionale delle Ricerche within the CRUI-CARE Agreement.

FUNDING INFORMATION

The research has been partially funded by project MIUR PRIN 2017 – Morphological Biomarkers for early diagnosis in Oncology (MORFEO) Prot. 2017N7R2CJ.

CONFLICT OF INTEREST

Authors have no conflicts of interest to declare.

PEER REVIEW

The peer review history for this article is available at <https://publons.com/publon/10.1002/cyto.a.24685>.

ORCID

Lisa Miccio  <https://orcid.org/0000-0001-9427-881X>

REFERENCES

1. Ferraro P, Wax A, Zalevsky Z. Coherent light microscopy. Berlin Heidelberg: Springer; 2011. p. 46.
2. Miccio L, Memmolo P, Merola F, Mugnano M, Ferraro P. Optobiology: live cells in optics and photonics. *J Phys Photon*. 2020;3(1):012003.
3. Pan T, Lu D, Xin H, Li B. Biophotonic probes for bio-detection and imaging. *Light Sci Appl*. 2021;10(1):124.
4. Gather MC, Yun SH. Single-cell biological lasers. *Nat Photon*. 2011; 5(7):406–10.
5. Miccio L, Memmolo P, Merola F, Netti PA, Ferraro P. Red blood cell as an adaptive optofluidic microlens. *Nat Commun*. 2015;6(1):6502.
6. Liu X, Li Y, Xu X, Zhang Y, Li B. Red-blood-cell-based microlens: application to single-cell membrane imaging and stretching. *ACS Appl Bio Mater*. 2019;2(7):2889–95.
7. Li Y, Liu X, Li B. Single-cell biomagnifier for optical nanoscopes and nanotweezers. *Light Sci Appl*. 2019;8(1):61.
8. Rodrigues de Mercado R, van Hoorn H, de Valois M, Backendorf C, Eckert J, Schmidt T. Characterization of cell-induced astigmatism in high-resolution imaging. *Biomed Opt Express*. 2022;13(1):464–73.

9. Jiang C, Yue H, Yan B, Yan B, Yan B, Dong T, et al. Label-free non-invasive subwavelength-resolution imaging using yeast cells as biological lenses. *Biomed Opt Express*. 2021;12(11):7113–21.
10. Go T, Kim JH, Byeon H, Lee SJ. Machine learning-based in-line holographic sensing of unstained malaria-infected red blood cells. *J Biophotonics*. 2018;11(9):e201800101.
11. Go T, Byeon H, Lee SJ. Label-free sensor for automatic identification of erythrocytes using digital in-line holographic microscopy and machine learning. *Biosens Bioelectron*. 2018;103:12–8.
12. Lee S, Park H, Kim K, Sohn Y, Jang S, Park Y. Refractive index tomograms and dynamic membrane fluctuations of red blood cells from patients with diabetes mellitus. *Sci Rep*. 2017;7(1):1039.
13. Mugnano M, Memmolo P, Miccio L, Merola F, Bianco V, Bramanti A, et al. Label-free optical marker for red-blood-cell phenotyping of inherited anemias. *Anal Chem*. 2018;90(12):7495–501.
14. Merola F, Barroso Á, Miccio L, Memmolo P, Mugnano M, Ferraro P, et al. Biolens behavior of RBCs under optically-induced mechanical stress. *Cytometry A*. 2017;91(5):527–33.
15. Viallat A, Abkarian M. Dynamics of blood cell suspensions in microflows. 1st ed. Boca Raton: CRC Press; 2019.
16. Cho S-Y, Gong X, Koman VB, Kuehne M, Moon SJ, Son M, et al. Cellular lensing and near infrared fluorescent nanosensor arrays to enable chemical efflux cytometry. *Nat Commun*. 2021;12(1):3079.
17. Doan M, Barnes C, McQuin C, Caicedo JC, Goodman A, Carpenter AE, et al. Deepometry, a framework for applying supervised and weakly supervised deep learning to imaging cytometry. *Nat Protoc*. 2021;16(7):3572–95.
18. Lau AKS, Shum HC, Wong KKY, Tsia KK. Optofluidic time-stretch imaging – an emerging tool for high-throughput imaging flow cytometry. *Lab Chip*. 2016;16(10):1743–56.
19. Wu J-L, Xu Y-Q, Xu J-J, Wei X-M, Chan AC, Tang AH, et al. Ultrafast laser-scanning time-stretch imaging at visible wavelengths. *Light Sci Appl*. 2017;6(1):e16196.
20. Chen X, Wu T, Gong Z, Guo J, Liu X, Zhang Y, et al. Lipid droplets as endogenous intracellular microlenses. *Light Sci Appl*. 2021;10(1):242.
21. Min J, Yao B, Trendafilova V, Ketelhut S, Kastl L, Greve B, et al. Quantitative phase imaging of cells in a flow cytometry arrangement utilizing Michelson interferometer-based off-axis digital holographic microscopy. *J Biophotonics*. 2019;12(9):e201900085.
22. Lee KCM, Wang M, Cheah KSE, Chan GCF, So HKH, Wong KKY, et al. Quantitative phase imaging flow cytometry for ultra-large-scale single-cell biophysical phenotyping. *Cytometry A*. 2019;95(5):510–20.
23. Singh DK, Ahrens CC, Li W, Vanapalli SA. Label-free fingerprinting of tumor cells in bulk flow using inline digital holographic microscopy. *Biomed Opt Express*. 2017;8(2):536.
24. Singh DK, Ahrens CC, Li W, Vanapalli SA. Label-free, high-throughput holographic screening and enumeration of tumor cells in blood. *Lab Chip*. 2017;17(17):2920–32.
25. Dannhauser D, Rossi D, Memmolo P, Finizio A, Ferraro P, Netti PA, et al. Biophysical investigation of living monocytes in flow by collaborative coherent imaging techniques. *Biomed Opt Express*. 2018;9(11):5194–204.
26. Dannhauser D, Rossi D, Memmolo P, Causa F, Finizio A, Ferraro P, et al. Label-free analysis of mononuclear human blood cells in microfluidic flow by coherent imaging tools. *J Biophotonics*. 2017;10(5):683–9.
27. Dannhauser D, Rossi D, Causa F, Memmolo P, Finizio A, Wriedt T, et al. Optical signature of erythrocytes by light scattering in microfluidic flows. *Lab Chip*. 2015;15(16):3278–85.
28. Steike DR, Hessler M, Korsching E, Lehmann F, Schmidt C, Ertmer C, et al. Digital holographic microscopy for label-free detection of leukocyte alternations associated with perioperative inflammation after cardiac surgery. *Cell*. 2022;11:755.
29. Tuchin V v. Advanced optical flow cytometry: Methods and disease diagnoses. Weinheim, Germany: Wiley-VCH; 2011.
30. Kreis T. Handbook of holographic interferometry. Weinheim, Germany: Wiley; 2004.
31. Pirone D, Sirico D, Miccio L, Bianco V, Mugnano M, Ferraro P, et al. Speeding up reconstruction of 3D tomograms in holographic flow cytometry via deep learning. *Lab Chip*. 2022;22(4):793–804.
32. Goodman JW. Introduction to Fourier optics. 4th ed. New York: W. H. Freeman; 2017.
33. Memmolo P, Distante C, Paturzo M, Finizio A, Ferraro P, Javidi B. Automatic focusing in digital holography and its application to stretched holograms. *Opt Lett*. 2011;36(10):1945.
34. Born M, Wolf E. Principles of optics electromagnetic theory of propagation, interference and diffraction of light. Oxford, United Kingdom: Pergamon; 1964.
35. Li Y. Focal shifts in diffracted converging electromagnetic waves I Kirchhoff theory. *J Opt Soc Am A*. 2005;22(1):68.
36. Běhal J, Bouchal Z. Optimizing three-dimensional point spread function in lensless holographic microscopy. *Opt Express*. 2017;25(23):29026.
37. Yu Y, Zappe H. Theory and implementation of focal shift of plasmonic lenses. *Opt Lett*. 2012;37(9):1592–4.
38. Mikš A, Novák J. Third-order aberration coefficients of a thick lens with a given value of its focal length. *Appl Optics*. 2018;57:4263–6.
39. Nissim N, Dudaie M, Barnea I, Shaked NT. Real-time stain-free classification of cancer cells and blood cells using interferometric phase microscopy and machine learning. *Cytometry A*. 2021;99A:511–23.
40. Raub CB, Nehmetallah G. Holography, machine learning, and cancer cells. *Cytometry A*. 2017;91A:754–6.
41. Holden E, Tarnok A, Popescu G. Quantitative phase imaging for label-free cytometry. *Cytometry A*. 2017;91A:407–11.
42. Kleiber A, Kraus D, Henkel T, Fritzsche W. Review: tomographic imaging flow cytometry. *Lab Chip*. 2021;21(19):3655–66.
43. Nitta N, Sugimura T, Isozak A, Mikami H, Hiraki K, Sukama S, et al. Intelligent image-activated cell sorting. *Cell*. 2018;175:266–76.
44. Isozaki A, Mikami H, Hiramatsu K, Sakuma S, Kasai Y, Iino T, et al. A practical guide to intelligent image-activated cell sorting. *Nat Protoc*. 2019;14:2370–415.
45. Nawaz AA, Urbanska M, Herbig M, Nötzel M, Kräter M, Rosendahl P, et al. Intelligent image-based deformation-assisted cell sorting with molecular specificity. *Nat Methods*. 2020;17:595–9.

How to cite this article: Běhal J, Pirone D, Sirico D, Bianco V, Mugnano M, del Giudice D, et al. On monocytes and lymphocytes biolens clustering by in flow holographic microscopy. *Cytometry*. 2023;103(3):251–9. <https://doi.org/10.1002/cyto.a.24685>